Electronic Materials Letters, Vol. 8, No. 6 (2012), pp. 595-603
DOI: 10.1007/s13391-012-2085-z

Crystallization Kinetics of Strontium Hexaferrite: Correlation to Structural, Morphological, Dielectric and Magnetic Properties

Ankush Thakur, R. R. Singh,* and P. B. Barman

Department of Physics, Jaypee University of Information Technology, Waknaghat, Solan 173234 (H.P.), India

(received date: 16 May 2012 / accepted date: 8 June 2012 / published date: December 2012)

Citrate precursor technique has been used to synthesize strontium hexaferrite and reported here. The crystallization process for ferrite phase formation has been investigated by TG/DTG/DTA for three different heating rates in air atmosphere. The thermal process mainly consists of three essential steps; first removal of water residues; second decomposition of organic compound and the third step is crystallization of $SrF_{12}O_{19}$. The activation energy of reaction is, 157 KJ/mole, evaluated using non-isothermal kinetic model. The precursor and crystallized $SrF_{12}O_{19}$ samples have been characterized for structural, chemical, morphological, dielectric and magnetic properties using x-ray diffraction (XRD), Fourier transform infrared spectroscopy (FTIR), field emission scanning electron microscopy (FESEM), inductance capacitance resistance (LCR) meter bridge and vibrating sample magnetometer (VSM) respectively. The degree of crystallization of $SrF_{12}O_{19}$ is the key factor for the dilution and enhancement of morphological and magnetic properties. The thermal, morphological and magnetic analysis confirms the formation of single phase of magnetoplumbite strontium ferrite at 1200°C.

Keywords: magnetic materials, DTA, x-ray diffraction, magnetic properties

1. INTRODUCTION

The strontium hexaferrite ($SrFe_{12}O_{19}$) is a hard magnetic material with magnetoplumbite structure.[1] This material has attracted much attention in past few decades due to their scientific and technological applications in the region of microwave to radio frequencies. This is due to high magnetocrystalline anisotropy, high Curie temperature, high electrical resistivity, high dielectric constant as well as high saturation magnetization and coercivity.[2-5] The dielectric and magnetic properties of ferrite materials in the nanoregime are significantly different from their bulk counterparts. *M*-type $SrFe_{12}O_{19}$ has a space group $P6_3/mmc$ and often expressed as RSR*S*. The S and R block stands for spinal and hexagonal structure. R* and S* are the blocks obtained by 180° rotation of R and S with respect to c-axis having equivalent atomic arrangements.[6,7] The hexagonal hard ferrite contains two 64 ions per unit cell on 11 different sites. The Fe^{3+} ions are distributed over five distinct crystallographic sites, three octahedral sites (12k, 2a, $4f_2$), one tetrahedral site ($4f_1$) and trigonal bipyramidal site (2b).[8] These crystallographic sites are coupled by O^{2-} ions to form collinear ferrimagnetic order and superexchange interaction between Fe^{3+}-O^{2-}-Fe^{3+}. The superexchange interaction and magnetocrystalline anisotropy are strongly depends upon the site occupation and different crystallographic site construct different role to dielectric and magnetic properties.

In this research work, citrate precursor technique for the synthesis of $SrFe_{12}O_{19}$ nanoparticles has been used. This method allows the subsequent crystallization to occur at low temperature, leading to formation of nanoparticles due to intimated mixing of staring materials on ionic levels and low cost technique for the mass production. The reaction kinetics for the prepared $SrFe_{12}O_{19}$ nanoparticles has been examined through differential thermal analysis using non-isothermal model. The effect of calcination temperature and crystallinity on the structural, morphological, dielectric and magnetic properties has been examined. Various parameters such as activation energy, particle size, dielectric constant, saturation magnetization and coercivity have been calculated.

2. EXPERIMENTAL PROCEDURE

Synthesis of strontium hexaferrite nanoparticles was accomplished in an aqueous reaction matrix containing ferric nitrate nonahydrate and strontium nitrate in the ratio Fe/Sr = 12. The pH of bath is adjusted to 6.5 with the help of ammonia solution. This ratio is according to composition of strontium ferrite, metal nitrates and citric acid monohydrate

*Corresponding author: raginirajsingh@gmail.com

were dissolved in the molar ratio 1.57. The precursor solution was evaporated at 70°C - 80°C for several hours under controlled and continuous magnetic stirring. The light weight brown colored powder was obtained during heating the viscous residual at 180°C. The obtained powder was further calcined at different temperatures for the formation of ferrite phase.

The thermal analysis for reaction kinetics and crystallization process of pure $SrFe_{12}O_{19}$ was performed by DTA (EXSTAR TG/DTA 6300), with a precursor sample placed in Al_2O_3 crucibles in the temperature range 30°C - 1430°C at three different heating rates. The crystal structure of prepared nanoparticles were analyzed with X'Pert Pro diffractometer in the range from 5° to 80° operating at 45 kV and 40 mA using a Cu-K_α radiation of wavelength 1.54 Å. The impact of heat treatment on structural morphology of prepared sample was probed by field emission scanning electron microscopy operating at an accelerating voltage of 20 kV. The FTIR-spectrometer (RZX-Perkin Elmer) was used for the detection of impurities and for the identification of metal oxygen stretching vibrations of hexaferrite. The FTIR-spectra of prepared samples were recorded in mid-infrared range (400 - 4000 cm^{-1}) by KBr method. The calcined powder sample was crushed and compressed using hydraulic compressor (10 ton) to form circular disc shaped pellet of the diameter 13 mm and thickness 1 mm. The dielectric measurements were performed on the pellet in the frequency range 100 to 10^5 Hz at room temperature using a HIOKI 3532-50 HITESTER LCR meter. The magnetic properties of samples were determined at room temperature from hysteresis loop using a vibrating sample magnetometer (Lakeshore 7410).

3. RESULTS AND DISCUSSION

3.1 Thermal analysis

The trace of DTA/DTG/TG for a precursor powder at the heating rate of 5 K/min in air atmosphere has been shown in Fig. 1(a). During the thermal analysis, it has been seen from the TG-curve that the weight loss of a precursor happens in three distinct steps in the temperature range from room temperature to 1430°C. The steps occurred at 74°C - 184°C, 330°C - 409°C and 640°C - 942°C respectively. The precursor exhibited a rapid weight loss up to 400°C indicating the hydroscopic nature. This weight loss can be attributed to the removal of water residues from macro and meso pores.[9] From 400°C to 942°C temperature range an additional weight loss (few amount) of a precursor has been observed. This can be credited to the combustion and decomposition of citrate precursor, and to the reaction of intermediates.[10,11]

The DTA-curve in Fig. 1(a) depicts both exothermic and endothermic effects of a precursor in the temperature range of 25°C - 1430°C. The DTA results are consistent with the

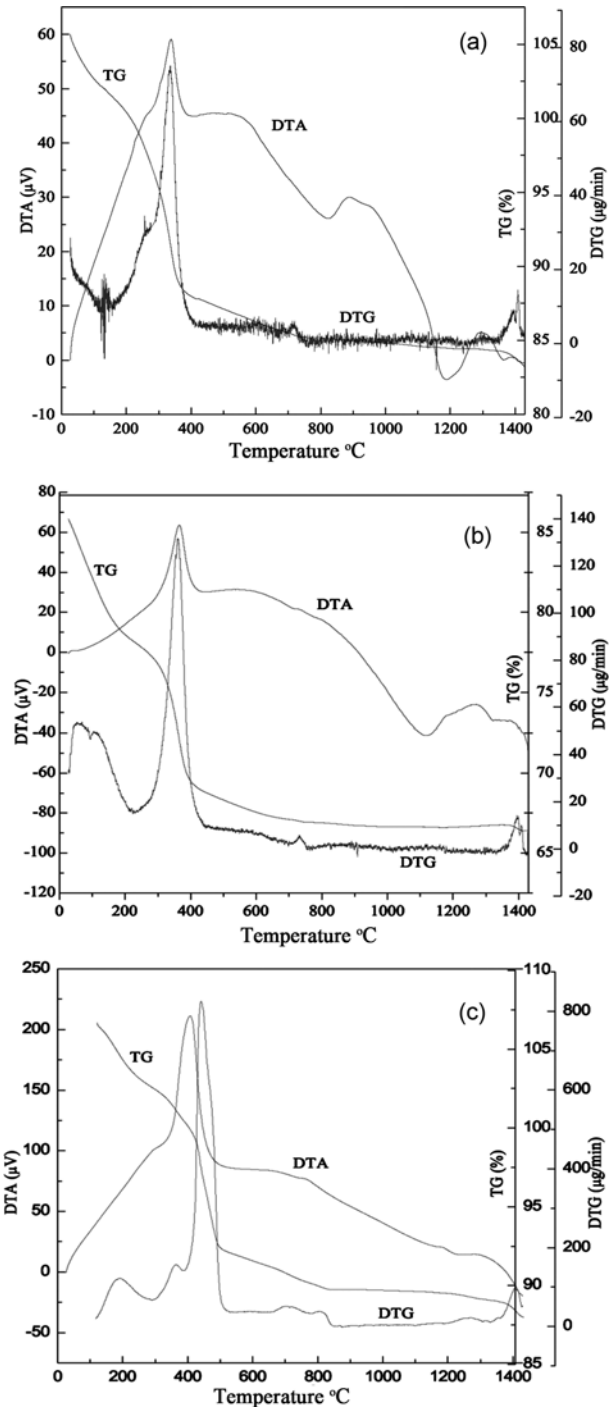

Fig. 1. TG/DTG/DTA curves of the precursor of strontium hexaferrite at different heating rates (a) 5 K/min, (b) 10 K/min, and (c) 50 K/min.

results of TG/DTG. The existence of an exothermic peak at the point of maximum weight loss i.e. 336°C (DTG) is related to decomposition of a precursor composed of citrate-nitrate gel. The formation of hexaferrite phase is not the single step reaction as observed in the case of spinal ferrite. Thermal analysis reveals that the formation takes place in

steps by means of endothermic reaction.[12] The existence of an endothermic peak at 824°C corresponds to the formation of $SrF_{12}O_{19}$ as well as intermediate phase. This has also been confirmed by the XRD analysis of a precursor powder calcined at 700°C and 800°C in air atmosphere. Above the second endothermic peak no further weight loss will be observed in TG-curve indicating the completion of reaction.[13]

To aid the further investigation of crystallization process, similar analysis have been carried out under same conditions except the heating rates, 10 and 50 K/min presented in Figs. 1(b) and 1(c) respectively. Similar behaviour has been observed for all the measurements with slight shift of DTA peaks to upward direction. It is concluded that for the different heating rates, there are different temperatures for the completion of reaction. The lower the heating rate; lower will be the reaction temperature. The present thermal investigations of a precursor powder at different heating rates will aid in the selection of reaction temperature with proper heating rate for formation of single phase strontium hexaferrite nanoparticles.

There are several models available for calculation of activation energy of crystallization process based on isothermal and non-isothermal processes. In present work we report, the kinetics of crystallization based on non-isothermal kinetic models *i.e.* Kissinger's method, Augis and Bennett's approximation and Matusita-Sakka's theory.[14-16] The Kissinger expressed the activation energy of the crystallization process of the prepared sample at crystallization temperature for the particular heating rates following equation using the Arrhenius and rate of crystallization equation:

$$\ln\frac{\beta}{T_C^2} = -\frac{E}{RT_C} + \ln\frac{AR}{E} \quad (1)$$

where β is the heating rate (K/min), T_C is the maximum peak temperature of DTA curve, E is the activation energy for the crystallization process, R is the universal gas constant (8.314 $Jmole^{-1}K^{-1}$) and A is the pre-exponential factor.

The plots of $\ln(\beta/T_c^2)$ against $\ln(1000/T)$ at different heating rates gives a straight line known as Kissinger's plot (Fig. 2(a)). Thus, the activation energy value has been obtained from slope of the straight line of these plots. The calculated value of activation energy for crystallization process of $SrFe_{12}O_{19}$ is, 157 KJ/mol. Activation energy have been verified by employing Augis-Bennett's approximation (Fig. 2(b)) Matusita-Sakka's theory (Fig. 2(c)) and non-isothermal kinetic models. The activation energy values determined

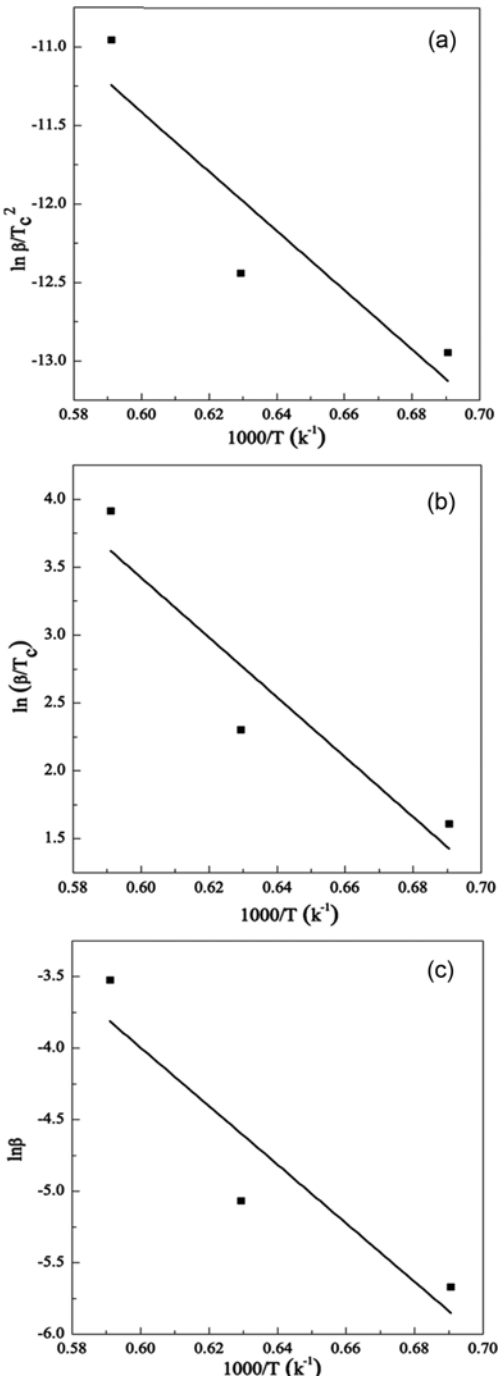

Fig. 2. (a) Kissinger's plot for the crystallization process of $SrFe_{12}O_{19}$, (b) Augis and Bennett's plot for the crystallization process of $SrFe_{12}O_{19}$, (c) Matusita-Sakka's plot for the crystallization process of $SrFe_{12}O_{19}$.

Table 1. Kinetic properties of $SrFe_{12}O_{19}$.

Sample	Heating rate (K)	T_C (K)	E (Kissinger) /kJmol^{-1}	E (Matusita) /kJmol^{-1}	E (Augis and Bennett) /kJmol^{-1}
$SrFe_{12}O_{19}$	5	1448	152	170	183
	10	1589			
	50	1692			

from these models are in close resemblance to each other as shown in Table 1.

3.2 X-ray diffraction

Crystallization process has been interpreted by means of x-ray diffraction studies; for this the precursor powder (A_0) has been further calcined for different temperature 700°C (A_1), 800°C (A_2) and 1200°C (A_3) at the heating rate of 5 K/min. The x-ray diffraction patterns of precursor and calcined powder A_3 have been presented in Fig. 3(a)-(b). The diffraction pattern of a precursor (Fig. 3(a)) shows broad peaks, indicating the presence of nanocrystalline phase. This can be attributed to the existence of organic compounds in precursor powder.[17] As the calcination temperature of precursor powder increases, the diffraction peak becomes narrower and intense representing enhancement of crystallite size and crystallinity respectively. The diffraction patterns of (not presented here) A_1 and A_2 samples shows the formation of ferrite phase along with the presence of secondary phases such as α (γ)-Fe_2O_3 and $SrFe_2O_4$.[18-20] The existence of secondary phases indicates the incomplete reaction between Fe^{3+} and Sr^{2+} under these synthesis conditions. The presence of α-Fe_2O_3 phase, means the system need longer and high calcination temperature for the completion of reaction. This is because, the crystal structure of α-Fe_2O_3 is orthorhombic hexahedron and difficult to convert into ferrite phase as compared to γ-Fe_2O_3.[21] The sample A_3 (Fig. 3(b)) represents the sharp, intense and narrower diffraction peaks, and disappearance of secondary phase indicating the formation of single phase *M*-type hexaferrite with high crystallinity. All the apparent peaks (110), (114), (107), (203), (205), (206), (208), and (303) in diffraction pattern have been similar to standard (*JCPDS:* 80-1198) diffraction pattern of hexagonal ferrite.

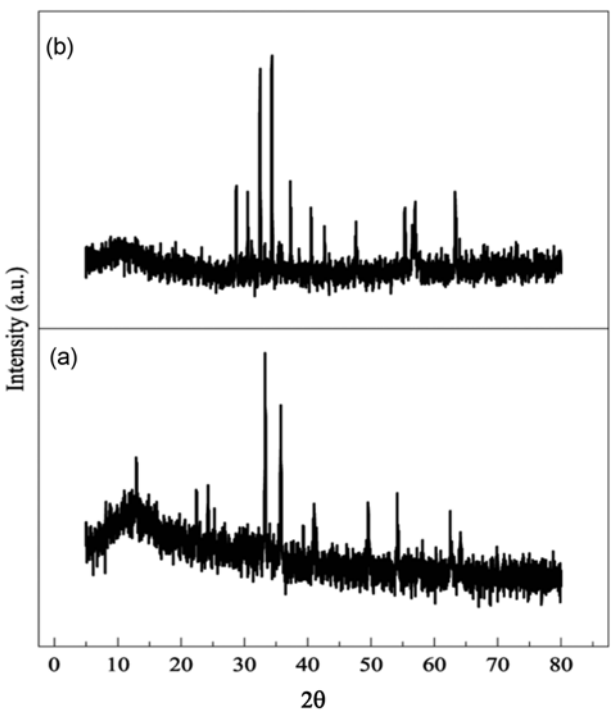

Fig. 3. X-ray diffraction patterns of (a) precursor powder and powder calcined at (b) 1200°C.

Table 2. Variation of crystallite size with calcination temperature.

Sample	2θ (°)	Crystallite size (nm)
700°	34.08	26.80
800°C	34.13	30.77
1200°C	34.32	69.28

The diffraction peak broadening technique has been employed for most intense (114) peak to calculate the crystallite size. The crystallite size for $SrFe_{12}O_{19}$ nanoparticles has been calculated using Scherrer's formula:[22,23]

$$D = k\lambda/\beta\cos\theta \quad (2)$$

where D is crystallite size, β is the full width at half maxima, θ is the angle of diffraction, k is the shape factor (0.9) and λ the wavelength of x-ray (1.5406 Å for Cu-Kα). The calculated crystallite size has been shown in Table 2 and it can be seen that the crystallite size increases with the increasing calcination temperature in the direction parallel to c-axis (114). The sample A_3 stands for maximum crystallite size but still smaller than the single domain crystal particle size ~270 nm as reported earlier.[24,25] The crystallinity and crystal growth of nanoparticles are closely related to calcination. The growth of crystallite size with increasing calcination temperature can be accredited to the fusion of nanoparticles with each other by melting their surfaces. The fusion of nanoparticles well below their melting point is owing to weak binding of surface atoms result in sharp decrease of surface melting point.[26,27]

3.3 Field emission-scanning electron microscope

The FESEM micrographs of sample calcined at different temperatures have been depicted in Fig. 4(a)-(c). The average grain size of strontium hexaferrite estimated from FESEM micrograph to be ~100 nm. FESEM micrograph for precursor has been presented in Fig. 4(a). It can be seen from the micrograph that the particles are embedded in a sheet like structure due to the presence of impurities or incomplete reaction in sample as confirmed from x-ray diffraction analysis. Small size particles are formed due to fragmentation of sheet like structure with the increase of calcination temperature may be the calcination is responsible for this. It is known that the microstructure of nanoparticles can be influenced and improved by heat treatment.[28] The sample calcined at 700°C becomes plate or needle like shape (Fig. 4(b)). This can be attributed to increase in crystallinity of particles, but morphology of particles still not flawless. It has

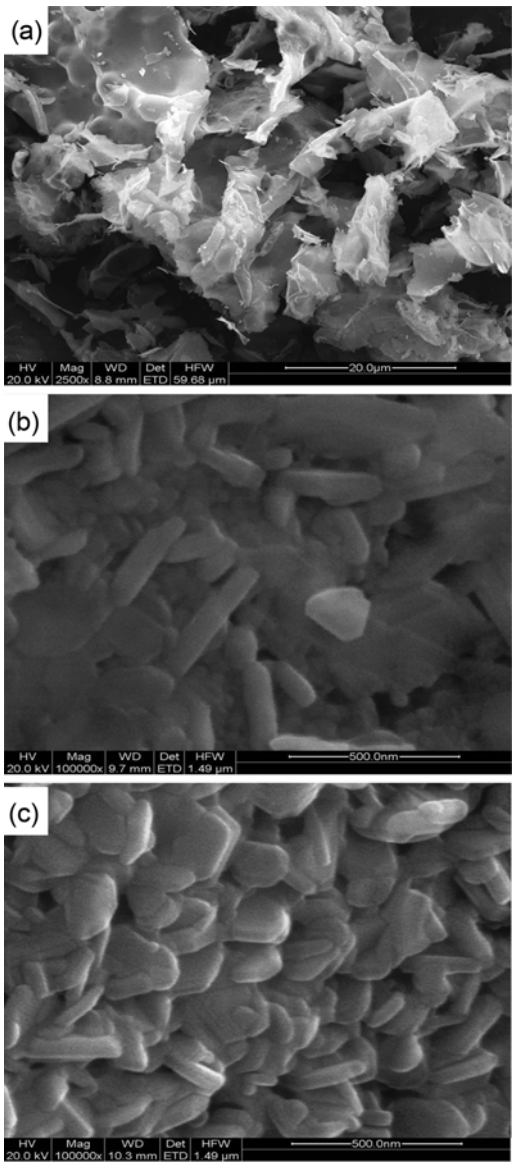

Fig. 4. FESEM micrographs of (a) precursor powder, (b) powder calcined at 700°C and (c) powder calcined at 1200°C.

also been observed from the micrograph that the particles exhibit porous and agglomerated microstructure. The ignition of sample causes evolution of large amount of gases during combustion or decomposition process and magnetic nature of particles has been responsible for high porosity and agglomeration respectively.[29,30] The calcination temperature mends the crystallinity of ferrite phase and can be describe in terms of Ostwald ripening.[31] Ostwald ripening is a process in which large number of nano particles are formed initially, but later only few of them remain which grow in size at the cost of smaller ones. The ultrafine and homogeneous particles have been formed with immaculate and well resolved hexagonal structure for the sample calcined at 1200°C (Fig. 4(c)).

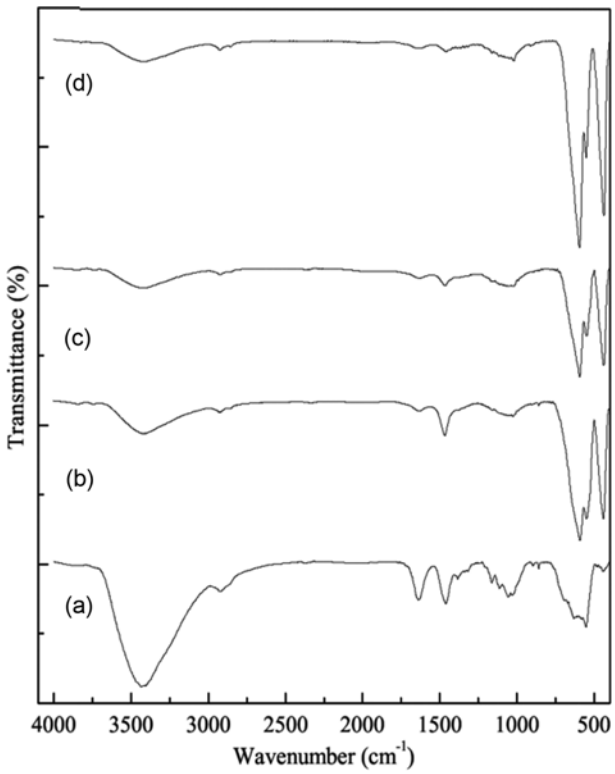

Fig. 5. FTIR-spectra (a) precursor powder and powder calcined at (b) 700°C, (c) 800°C, (d) 1200°C.

3.4 Fourier transform infrared spectroscopy

The FTIR-spectra of a precursor and calcined powder are shown in Fig. 5(a)-(d). FTIR-spectrum of a precursor in Fig. 5(a) shows that the characteristic bands have appeared in the range of 3200 - 3270 cm^{-1} and 1638 cm^{-1}. These bands are assigned to be hydroxyl and carboxyl group of citric acid respectively.[32,33] The absorption peak at 1059 cm^{-1} corresponds to C-O stretching vibration of C-O-H band. Frequency bands near 1460.37 cm^{-1}, 1383.59 cm^{-1} and 858.82 cm^{-1} are attributed to nitrate ions.[34] After the calcination of precursor at 700°C, peak appears at 1465.72 cm^{-1} in Fig. 5(b) and is ascribed to absorption of strontium carbonate bands.[35,36] The observed absorption bands in the range 400 - 800 cm^{-1} are due to iron oxide.[20,37-39] The absorption band at 2916.52 cm^{-1} arise from Fermi resonance between stretching vibration of O-H band and combination of frequency of stretching vibration of C-O and bending vibration of C-O-H band.[11] The metal-oxygen stretching bands are prominent and other bands start decreasing but still persist (Fig. 5(c)) after heating the precursor powder at 800°C. Characteristic bands of CO_2^- group and NO_3^- ions have been diminished after heating the sample to 1200°C which shows the completion of redox reaction in which citrate ions act as reductant and nitrate ions as oxidant.[32,33] A new set of completely resolved bands have been appeared (Fig. 5(d)) at wavenumber of 435.05, 551.04 and 594.26 cm^{-1}

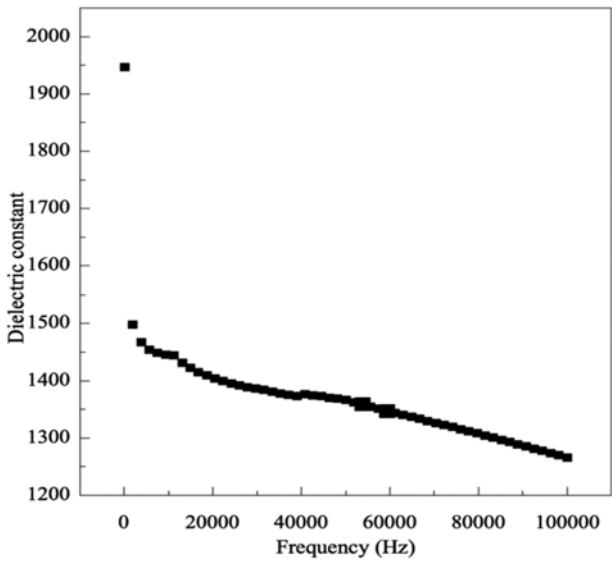

Fig. 6. Plot of dielectric constant as function of frequency at room temperature for powder calcined at 1200°C.

and identified as stretching vibration of metal-oxygen bond indicating the formation of hexaferrite.[20,34,40]

3.5 Dielectric properties

The principle of parallel plate capacitor has been employed to calculate the dielectric parameters in the frequency range 100 to 10^5 Hz at room temperature using following equation:

$$\varepsilon = Cd/\varepsilon_0 A \quad (3)$$

where C is the capacitance of the pellet, ε_o is the permittivity of free space, A is the area of cross-section and d is the thickness of pellet. The variation of dielectric constant (ε) with frequency at room temperature has been shown in Fig. 6. ε of $SrF_{12}O_{19}$ has been found to decrease with increasing frequency. This is the normal behavior of ferrite and can be attributed to surface charge polarization.[41] According to Maxwell-Wagner and Koops theory, the dielectric structure of ferrite system can be considered as heterogeneous system.[41-43] The heterogeneous system of dielectric materials is assumed to consist of highly conductive layer of grains separated by poor conductive grain boundaries. In nanometric dimensions heterogeneous structure of ferrite materials play a vital role in determining the dielectric properties. The grain boundaries in sample have been associated with grain size; small grain size will have large number of grain boundaries and vice versa. Dielectric constant (ε) of $SrF_{12}O_{19}$ ferrite shows higher value at low frequency and this can be explained on the basis of crystallite size and defects in system. In the present work, the average crystallite size of $SrF_{12}O_{19}$ calcined at 1200°C is about 100 nm. This larger grain size results in fewer grain boundaries. The fewer grain boundaries and predominance of voids along with dislocations and Fe^{2+} ions in ferrite sample have been found responsible for high dielectric constant value at low frequency.[44-46]

The dielectric polarization in ferrite system is similar to mechanism of electrical conduction *i.e.* the electronic exchange between ferrous and ferric ions at the octahedral sites. The exchange of electron in ferrite system has been responsible for dielectric polarization *i.e.* the displacement of electrons in the direction of electric field. The dielectric polarization reduces the inside electric field of the ferrite. As a consequence, the dielectric constant decreases with increase in frequency. The decrease of dielectric constant is attributed to the fact that beyond the certain frequency of external electric field, the electronic exchange between the ferrous and ferric ions cannot follow the applied electric field.[43,47]

3.6 Magnetic properties

The magnetic properties of a precursor and calcined powder have been measured from hysteresis loops and can be seen in Fig. 7. The magnetic properties of ferrite system are influenced by chemical composition, calcination temperature, impurities, and morphology as well as preparation technique.[48] The measured values are listed in Table 3. It is observed from Fig. 7(d) that the magnetic properties perk up as the calcination temperature increases and the optimum values for prepared $SrFe_{12}O_{19}$ have been obtained for the sample calcined at 1200°C. The continuous improvement in magnetic parameters can be indorsing to the progressive reaction between un-reacted constituents of iron oxide and non-ferromagnetic monoferrite to form 100% single phase hexaferrite, as discussed above the crystallinity increases with calcination. The low H_C and M_S value of a precursor powder corresponds to the presence of γ-Fe_2O_3 and non-magnetic phase of strontium oxide respectively.[20] The improvement in crystallinity, phase homogeneity and increase in magnetic domain size of particles result in the alignment of magnetic spins along the direction of applied field,[26] and as a consequence the magnetization and coercivity value increases.[49,50] The obtained optimum results for sample calcined at 1200°C are consistent with the thermal analysis indicating the formation of pure magnetoplumbite phase.

The variation of coercivity (reverse magnetic field to demagnetize the nanoparticles) with crystallite size has been shown in Fig. 8. According to Stoner-Wohlfarth single domain theory the coercivity for single domain nanoparticles is approximated by:[51]

$$H_C = 2K/\mu_0 M_S \quad (4)$$

where K is the magnetocrystalline anisotropy and μ_o is the permeability of free space. H_C is directly proportional to

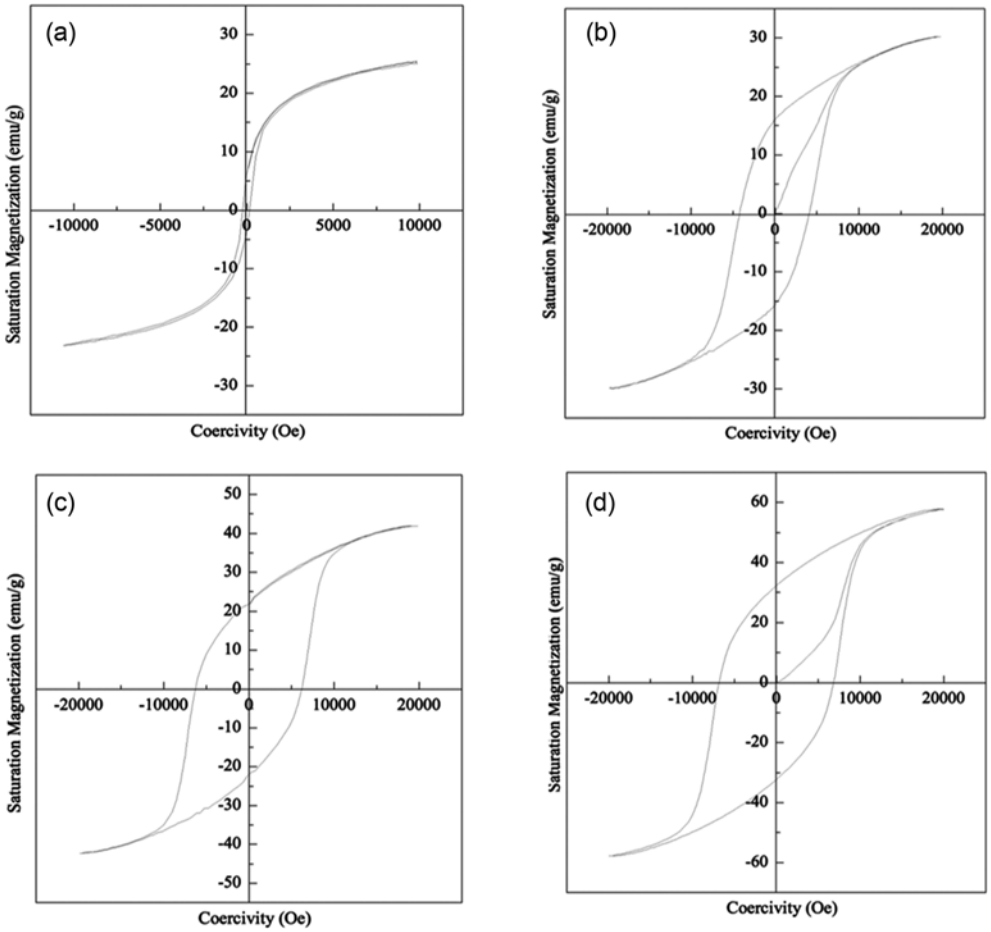

Fig. 7. Hysteresis loops for (a) precursor powder and powder calcined at (b) 700°C, (c) 800°C, (d) 1200°C.

Table 3. Magnetic properties of $SrFe_{12}O_{19}$.

Sample	M_S (emu/g)	H_C (Oe)
Precursor	25.46	232.8
700°C	30.17	4272.34
800°C	41.98	6235.75
1200°C	57.76	6828.54

energy barrier according to the equation:[49]

$$E_A = KV\sin^2\theta \quad (5)$$

where V volume of nanoparticle, E_A is the energy barrier and θ is the angle between the applied field and easy axis of the nanoparticle. The E_A is also proportional to V under the same magnetization direction and thus, the coercivity of nanoparticles is closely related to crystallite size. The increment in coercivity of hexaferrite nanoparticles with an increase of crystallite size can be explained on basis of Herzer theory.[52] According to Herzer theory, the coercivity of nanoparticles is proportional to D^6 when the crystallite size is within the range

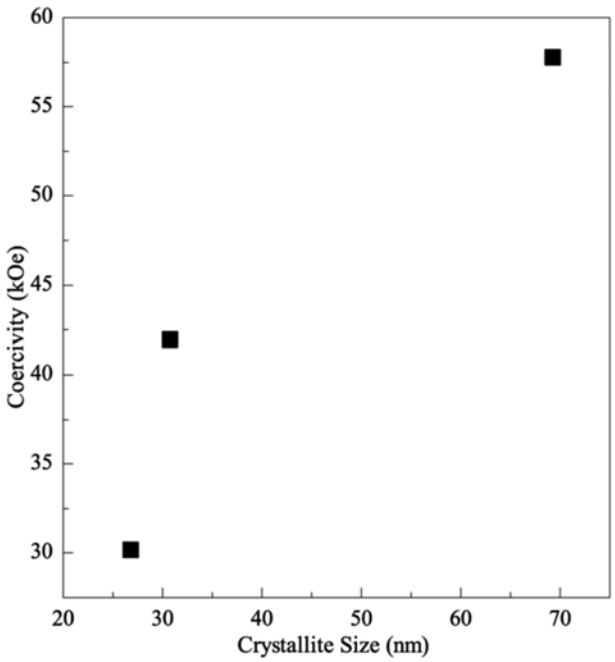

Fig. 8. The coercivity of $SrFe_{12}O_{19}$ as a function of crystallite size.

of single domain size and inversely proportional to D for multi-domain sized particle.

4. CONCLUSIONS

Hexagonal shaped nanoparticles (69 nm) of $SrF_{12}O_{19}$ have been successfully synthesized when the precursor is calcined at 1200°C for 4 h, using citrate precursor technique. The morphology and crystallite size are strongly influenced by the calcination temperature. The DTA technique reveals that the highly crystalline nanoparticles are formed by the endothermic reaction. The reaction kinetics for the crystallization process of $SrF_{12}O_{19}$ yielded overall activation energy of 157 kJ/mole using Kissinger's non-isothermal model. The crystallization involves the weight loss of a precursor in three distinct steps. The intense weight loss in the temperature range 30 - 400°C indicates the hydroscopic nature. The formation of ferrite phase was followed by reaction between intermediates rather than single step formation. The average crystallite size of $SrF_{12}O_{19}$ nanoparticles measured from FESEM is larger than the crystallite size calculated from x-ray peak broadening technique. This is attributed that the SEM gives the size of secondary particles rather than size of primary particles. The dielectric constant (ε) of $SrF_{12}O_{19}$, in the frequency range of 100 Hz to 10^5 Hz has studied. The dielectric constant value is higher at low frequency as compared to high frequency and found to be decrease with an increase of frequency. The dielectric behaviour of ferrite can be explained on the basis of Maxwell-Wagner and Koops Phenomenological theory. The space charger carriers aligned themselves at the grain boundaries due to the resistance offered by grain boundaries. The local displacement of electrons resulting in polarization of dielectric medium that leads to high value of ε. The magnetic parameters are closely related to the crystallinity of particles. It is found that the sample calcined at 1200°C have higher M_S and H_C value while comparing with sample calcined at 700°C. This improvement in hysteresis is considered to be the progressive reaction of intermediates with the calcination temperature. The prepared strontium hexaferrite nanoparticles with preeminent hexagonal crystal structure and size are used as a dielectric or magnetic filler to minimize the electromagnetic interference. The high coercivity and single domain sized nanoparticles can be aid to obtained desired signal to noise ratio (SNR) which can be used for high density perpendicular recording media.

REFERENCES

1. X. S. Liu, L. F. Garcia, F. Hu, D. R. Zhu, M. Suarez, and J. L. Menendez, *Mater. Chem. Phys.* in press (2012). [DOI: 10.1016/j.matchemphys.2012.01.123]
2. Y. Ebrahimi, A. A. S. Alvani, A. A. Sarabi, H. Sameie, R. Salimi, M. S. Alvani, and S. Moosakhani, *Ceram. Int.* in press (2012). [DOI:10.1016/j.ceramint.2012.01.040]
3. S. M. Masoudpanah, S. A. S. Ebrahimi, and C. K. Ong, *J. Magn. Magn. Mater.* **324**, 1440 (2012).
4. A. Davoodi and B. Hashemi, *J. Alloys Compd.* **512**, 179 (2012).
5. Z. Zhang, X. Liu, X. Wang, Y. Wu, and R. Li, *J. Alloys Compd.* **525**, 114 (2012).
6. A. Haq and M. A. U. Rehman, *Physica B* **407**, 822 (2012).
7. G. M. Rai, M. A. Iqbal, and K. T. Kubra, *J. Alloys Compd.* **495**, 229 (2010).
8. R. M. Almeida, W. Paraguassu, D. S. Pires, R. R. Correa, and C. W. de Araujo Paschoal, *Ceram. Int.* **35**, 2443 (2009).
9. R. D. C. Lima, M. S. Pinho, and T. Ogasawara, *J. Therm. Anal. Calorim.* **97**, 131 (2009).
10. N. Chakrabarti and H. S. Maiti, *Matter. Lett.* **30**, 169 (1997).
11. W. Zhao, Q. Zhang, and J. Guan, *J. Wuhan. Univ. Technol.* **21**, 36 (2006).
12. S. Tyagi, R. C. Agarwala, and V. Agarwala, *J. Mater. Sci. Mater. Electron.* **22**, 1085 (2011).
13. M. J. Iqbal and S. Farooq, *Mater. Res. Bull.* **46**, 662 (2011).
14. H. E. Kissinger, *Anal. Chem.* **29**, 1702 (1957).
15. J. A. Augis and J. E. Benett, *J. Thermal. Anal.* **13**, 283 (1978).
16. K. Matusita and S. Sakka, *Phys. Chem. Glasses.* **20**, 81 (1979).
17. H. Shang, J. Wang, and Q. Liu, *Mater. Sci. and Eng. A.* **456**, 130 (2007).
18. C. L. Yuan, Y. S. Hong, and C. H. Lin, *J. Magn. Magn. Mater.* **323**, 1851 (2011).
19. W. Zhanyong, Z. Liuming, L. Jieli, Q. Huichun, Z. Yuli, F. Yongzheng, J. Minglin, and X. Jiayue, *J. Magn. Magn. Mater.* **322**, 2782 (2010).
20. A. Mali and A. Ataie, *Scr. Mater.* **53**, 1065 (2005).
21. J. Qiu, L. Liang, and M. Gu, *Mater. Sci. and Eng. A.* **393**, 361 (2005).
22. M. J. Iqbal, R. A. Khan, S. Mizukami, and T. Miyazaki, *Mater. Res. Bull.* **46**, 1980 (2011).
23. M. J. Iqbal and S. Farooq, *J. Alloys Compd.* **505**, 560 (2010).
24. Q. Fang, H. Cheng, K. Huang, J. Wang, R. Li, and Y. Jiao, *J. Magn. Magn. Mater.* **294**, 281 (2005).
25. D. Y. Chen, Y. Y. Meng, D. C. Zeng, Z. W. Liu, H. Y. Yu, and X. C. Zhong, *Mater. Lett.* in press (2012). [DOI: 10.1016/j.matlet.2012.02.078]
26. V. Kumar, A. Rana, M. S. Yadav, and R. P. Pant, *J. Magn. Magn. Mater.* **320**, 1729 (2008).
27. Y. Matsuo, K. One, T. Hashimoto, and F. Nakao, *IEEE Trans. Magn.* **37**, 2369 (2001).
28. C. Doroftei, E. Rezlescu, P. Dorin, and N. Rezlescu, *Cryst. Res. Technol.* **41**, 1112 (2006).
29. L. Mingquan, S. Fuzhan, S. Xiangqian, and Z. Yongwei, *J.*

Sol-Gel Sci. Technol. **56**, 39 (2010).
30. Z. Durmus, H. Kavas, H. Sozeri, M. S. Toprak, A. Aslan, and A. Baykal, *J. Supercond. Nov. Magn.* (In Press). [DOI:10.1007/s10948-011-1396-x]
31. W. Z. Ostwald, *Phys. Chem.* **34**, 495 (1900).
32. M. G. Hasab, S. A. S. Ebrahimi, and A. Badiei, *J. Magn. Magn. Mater.* **316**, e13 (2007).
33. M. G. Hasab, S. A. S. Ebrahimi, and A. Badiei, *J. Eur. Ceram. Soc.* **27**, 3637 (2007).
34. F. Song, X. Shen, J. Xiang, and H. Song, *Mater. Chem. Phys.* **120**, 213 (2010).
35. X. Shen, M. Liu, F. Song, and X. Meng, *J. Sol-Gel Sci. Technol.* **53**, 448 (2010).
36. X. Wang, D. Li, L. Lu, and X. Wang, *J. Alloys Compd.* **237**, 45 (1996).
37. M. J. Iqbal, M. N. Ashiq, and I. H. Gul, *J. Magn. Magn. Mater.* **322**, 1720 (2010).
38. J. Qiu, L. Liang, and M. Gu, *Mater. Sci. and Eng. A.* **393**, 361 (2005).
39. F. Y. Hsuan and C. L. Pei, *J. Alloys Compd.* **416**, 222 (2006).
40. M. N. Ashiq, M. J. Iqbal, and I. H. Gul, *J. Alloys Compd,* **487**, 341 (2009).
41. C. G. Koops, *Phys. Rev.* **83**, 121 (1951).
42. J. C. Maxwell, *A Treatise on Electricity and Magnetism*, p. 752, Oxford Univ. Press, Oxford (1929).
43. K. W. Wagner, *Ann. Phys.* **40**, 817 (1913).
44. M. N. Ashiq, M. J. Iqbal, and I. H. Gul, *J. Magn. Magn. Mater.* **323**, 259 (2011).
45. K. M. Batoo, S. Kumar, and C. G. Lee, Alimuddin, *Curr. Appl. Phys.* **9**, 826 (2009).
46. S. M. Ramey, S. A. Siddiqi, S. Atiq, M. S. Awan, and S. Riaz, *Chin J. Chem. Phys.* **23**, 591 (2010).
47. M. A. Ahmed, N. Okasha, and R. M. Kershi, *Mater. Chem. Phys.* **113**, 196 (2009).
48. C. Sudakar, G. N. Subbanna, and T. R. N. Kutty. *J. Electroceram* **6**, 123 (2001).
49. L. Ai and J. Jiang, *J. Mater. Sci. Mater. Electron.* **20**, 257 (2009).
50. P. Xu, X. Han, and M. Wang, *J. Phys. Chem. C,* **111**, 5866 (2007).
51. E. C. Stoner and E. P. Wohlfarth, *IEEE Trans. Magn.* **27**, 3475 (1991).
52. G. Herzer, *Mater. Sci. Eng. A*, **133**, 1 (1991).